Supplement of Weather Clim. Dynam., 7, 263–275, 2026
https://doi.org/10.5194/wcd-7-263-2026-supplement

Supplement of

Mediterranean Sea heat uptake variability as a precursor to winter precipitation in the Levant

Ofer Cohen et al.

Correspondence to: Ori Adam (ori.adam@mail.huji.ac.il)

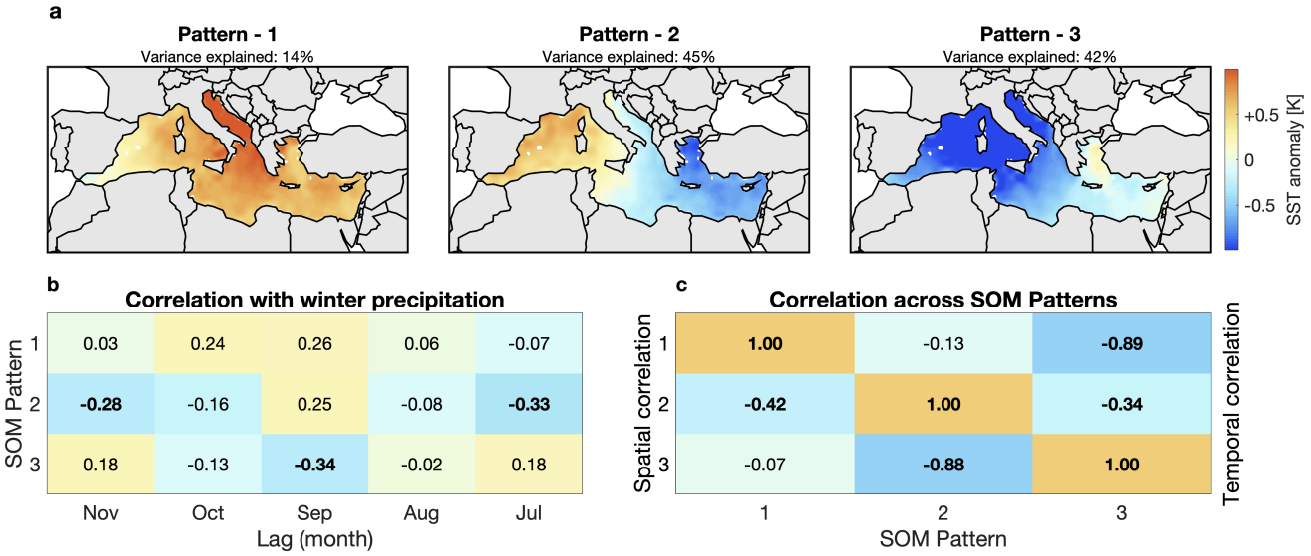

Figure S1. (a) Mediterranean monthly SST anomalies from 1979 to 2023 clustered into three SOM patterns; (b) Lagged correlation of the loading of each monthly SST SOM pattern during the months July–November with mean Levant winter (DJF) land precipitation; (c) Spatial correlations between the SOM patterns (below diagonal) and temporal correlations between the loading time series of the SOM patterns (above diagonal). Pearson correlation coefficients significant at the 5% level are bolded. The variance explained by each SOM pattern refers to the temporal variance explained by each pattern. The total variance explained by the three patterns, which takes into account the pattern frequency, is 37%. Data taken from ERA5 for 1979–2023.

S1 SOM analysis

To ensure the robustness of our results, in addition to the EOF analysis, we also analyzed the dominant spatiotemporal patterns of variability in Mediterranean SST and ocean heat uptake (Q_f) using Self-Organizing Maps (SOM) analysis. The sea surface fields (both SST and ocean heat uptake) were masked to exclude land areas, ensuring that our analysis focuses solely on the Mediterranean ocean. Then, the anomaly from climatology is calculated, and the fields are detrended to exclude the effect of climate change from our analysis.

The SOM algorithm is used for projecting high-dimensional input data onto a lower-dimensional grid (typically two-dimensional). As the input data is presented to the SOM network, the algorithm identifies the Best Matching Unit (BMU), which is the node (or neuron) on the grid whose weight vector most closely resembles the input data. The SOM network then adjusts the weight vectors of the BMU and its neighboring nodes to better match the input data. This iterative process of competitive learning continues until the SOM stabilizes after the training epochs are over, clustering similar data points together and preserving the topological relationships of the input space.

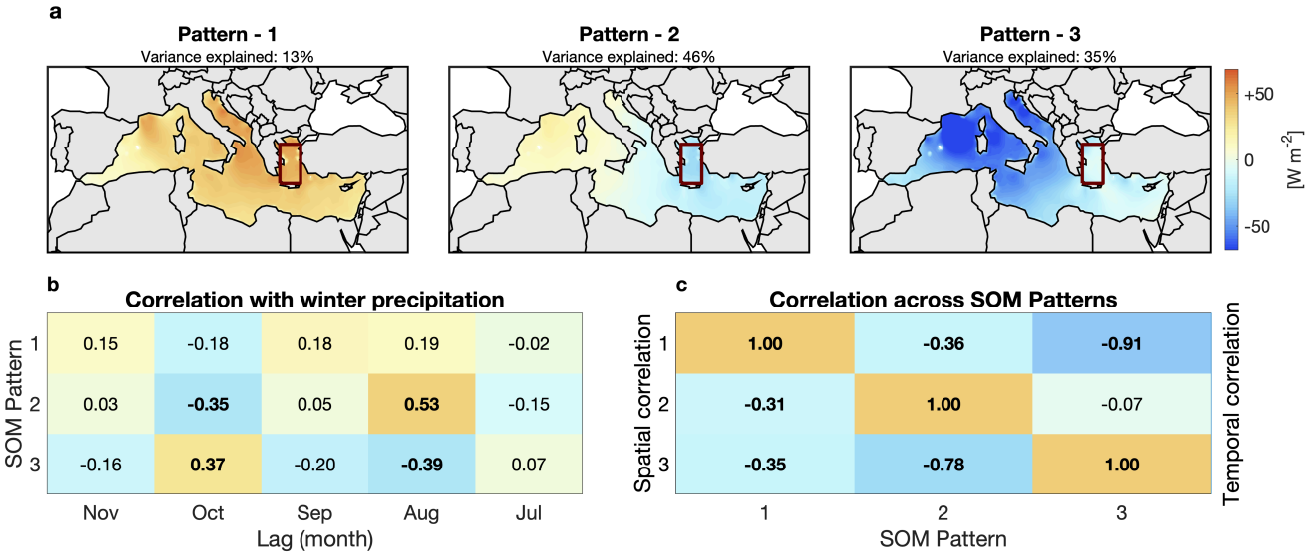

Figure S2. (a) Mediterranean monthly Q_f anomalies from 1979 to 2023 clustered into three SOM patterns. Red rectangle indicates region used to calculate the Aegean Q_f Anomaly index (AQA, defined in section **??**). (b) Lagged correlation of the loading of each monthly Q_f SOM pattern during the months July–November with mean Levant winter (DJF) land precipitation; (c) Spatial correlations between the SOM patterns (below diagonal) and temporal correlations between the loading time series of the SOM patterns (above diagonal). Pearson correlation coefficients significant at the 5% level are in bold. The variance explained by each SOM pattern refers to the temporal variance explained by each pattern. The total variance explained by the three patterns, which takes into account the pattern frequency, is 35% (see Supplementary Materials Figure S1). Data taken from ERA5 for 1979–2023.

We select the parameters and structure used in the SOM analysis to minimize the mean total topographic error (Figure S4), and to maximize the amount of variance explained by the SOM structure as a whole and by each individual SOM pattern (Figures S3 and S5). We note that the SOM analysis does not aim to necessarily maximize the amount of variance explained by the SOM structure, and take that into account in our selection process. Additionally, we try to minimize the overall number number of patterns to identify the most dominant modes, and also aim to minimize the repetitions of very similar spatial patterns when choosing our SOM configuration. Specifically, we experiment with different network configurations and parameters looking for patterns identified by SOM that are statistically robust. The results proved insensitive to the parameters used in the analysis (such as the Neighborhood function, the initialization scheme, and the number of iterations). Furthermore, increasing the number of SOM patterns does not increase their lagged predictive skill, and leads to repetition redundancy in the patterns. The final parameters used in our SOM analysis are detailed in Table S1. The resulting SOM patterns are analyzed to discern their spatial characteristics and temporal frequency, as well as the temporal variance they explain (Figures S1 and S2).

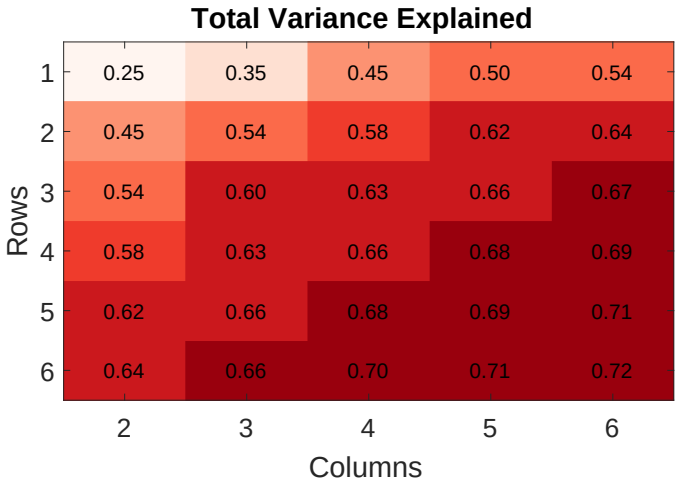

Figure S3. The calculated total variance explained by different SOM structures

The resulting optimal SOM structure is of 1 row and 3 columns (Table S1), explaining 35% of the variance of the data (Figures S3 and S5) with minimal pattern redundancy.

Parameter description	**Value**
Number of rows	1
Number of columns	3
Neighborhood function	Epanechnikov (ep)
Number of rough training iterations	5
Number of fine-tune training iterations	30
Neighborhood function initial radius	3
Neighborhood function final radius	1
Weight during mapping	2
Initialization scheme	Linear

Table S1. Parameters used in the SOM analysis.

The SOM patterns for SST and Q_f are highly similar, allowing their joint analysis. SOM pattern 1 explains 14% of SST temporal variance and 13% of Q_f temporal variance, and can be described as generally capturing a gradient between the central Mediterranean and its eastern and western parts. Using the loading time-series for each SOM pattern, measuring the association of each timestep in our data with the specific pattern, we can analyze their correlations to winter precipitation in the Levant and their temporal characteristics. Accordingly, the first SOM pattern of both SST and Q_f does not show a significant lagged correlation to Levant precipitation (Figures S1b and S2b), and is therefore not further analyzed.

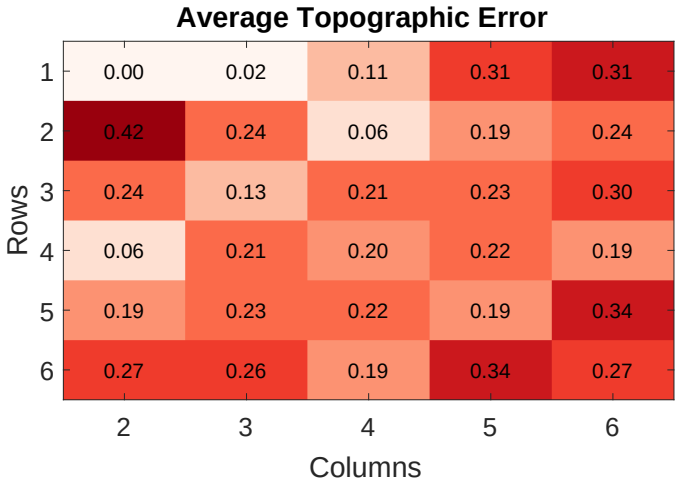

Figure S4. The average topographic error for different SOM structures.

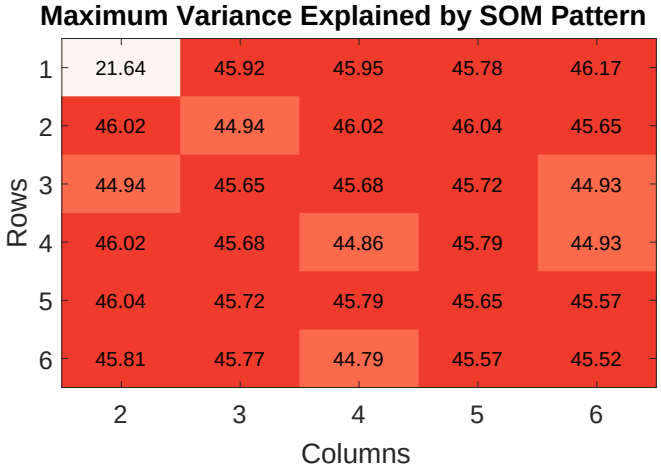

Figure S5. The maximum variance explained by a specific SOM pattern in different SOM structures.

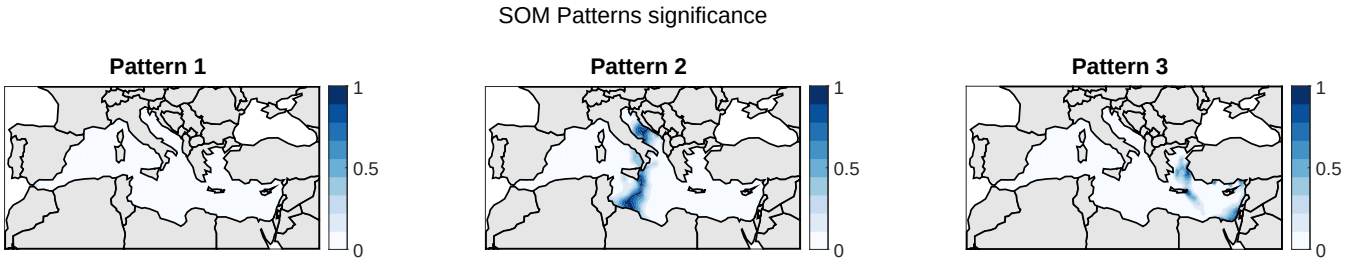

Figure S6. The spatial significance of the three Q_f SOM patterns, calculated by using Student's *t*-test. The maps plot the p-values for the patterns in each location, meaning low values ($<< 1$) indicate statistically significant regions.

The second and third SOM patterns of SST and Q_f, which account for most of the temporal variance (45% and 42% for SST and 46% and 35% for Q_f, respectively), generally capture east-west gradients across the Mediterranean basin (Figures S1a and S2a). Specifically, Pattern 2 features a surface anomaly located between the Ionian and Tyrrhenian Seas (i.e., east and west of Sicily); Pattern 3 exhibits a pronounced gradient between the western Mediterranean and the Aegean Sea. For both SST and Q_f, Patterns 2 and 3 have significant lagged correlations with Levant winter precipitation (peaking during November, September, and July for SST, and during October and August for Q_f), showing potential for sub-seasonal to seasonal prediction (Figures S1b and S2b). Consistent with Eq. (1) in the main text, since Q_f drives variations in SST, the peak correlation of Q_f is observed to lag that of SST by an additional month. Moreover, despite this extended lag, the highest correlation with Levant precipitation is found for Pattern 2 of Q_f in August ($R = 0.53$).

The spatial correlations across the SOM patterns and the temporal correlations across the loading time series of the SOM patterns are shown in Figures S1c and S2c. For both Q_f and SST, Patterns 2 and 3 are strongly spatially correlated ($|R| \geq 0.78$) but relatively weakly temporally correlated ($|R| \leq 0.36$), indicating that despite their topographical similarities, these patterns vary on different timescales.

To ensure the robustness of the SOM patterns, we also calculated the statistical significance of the SOM Patterns in relation to the data, using Student's *t*-test (Figure S6). We find that all 3 Q_f SOM patterns are significant over the majority of the Mediterranean, with the second pattern showing insignificant values in the central Mediterranean, and the third pattern showing slightly less significant values in the eastern Mediterranean (S6).

S2 Aegean Sea SST anomaly

Since SST is easier to measure than ocean heat uptake, we also assessed the connection between Aegean Sea SST anomaly and Levant winter precipitation. Figure S7a depicts the mean spatial pattern of SST for positive Aegean Sea SST anomaly months minus negative SST anomaly months, showing warmer sea surface conditions in the eastern Mediterranean highlighted in the Aegean and the Black Seas. Using the detrended monthly SST anomaly from seasonality in the Aegean Sea, we find that the anomaly is significantly correlated to the first and second SST SOM patterns (Figure S7b). Using the Aegean Sea SST anomaly index shown in Figure S8 we can calculate the correlation between the SST anomaly in the Aegean Sea and winter precipitation in the Levant. In Figure S7c, we show that the correlations are significant for July SST anomalies and ERA5 Levant winter precipitation, but not significant for precipitation measurements over Israel. Also, the correlations are weaker than those found for AQA, suggesting ocean heat uptake has a higher predictive power in the region. Following these findings, we chose to focus our analysis on Aegean Sea ocean heat uptake anomalies and their predictive abilities for winter precipitation in the Levant.

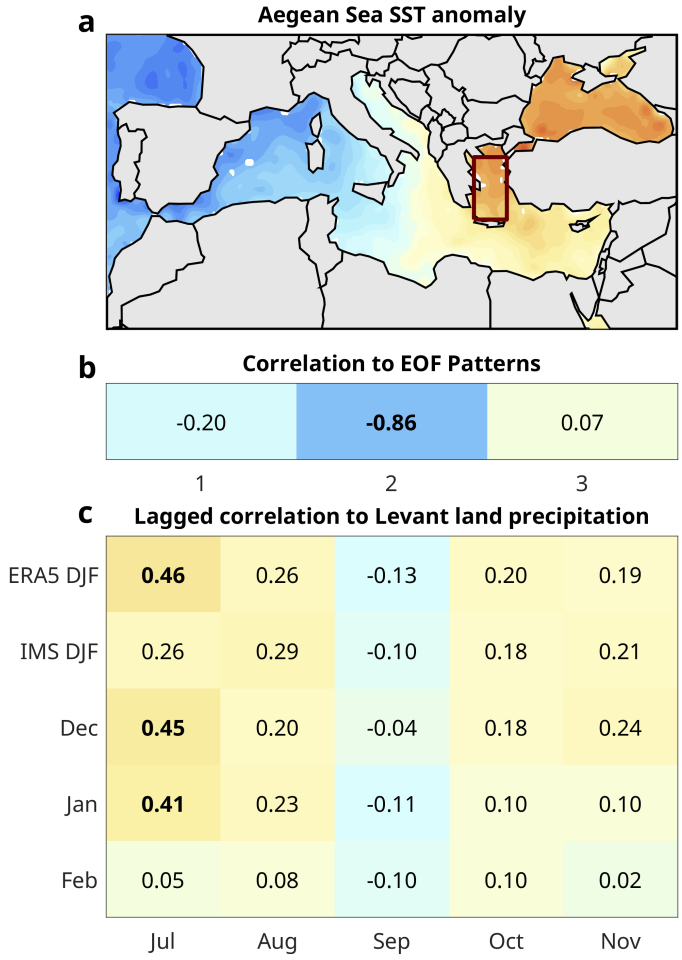

Figure S7. Aegean Sea SST anomaly; (a) depicts the SST anomaly for positive minus negative Aegean SST anomaly; (b) Correlation of the Aegean Sea SST anomaly Index to the SST EOF patterns; (c) Correlations between Aegean Sea SST anomaly and Levant winter precipitation.

S3 Extended AQA correlations to Levant winter precipitation

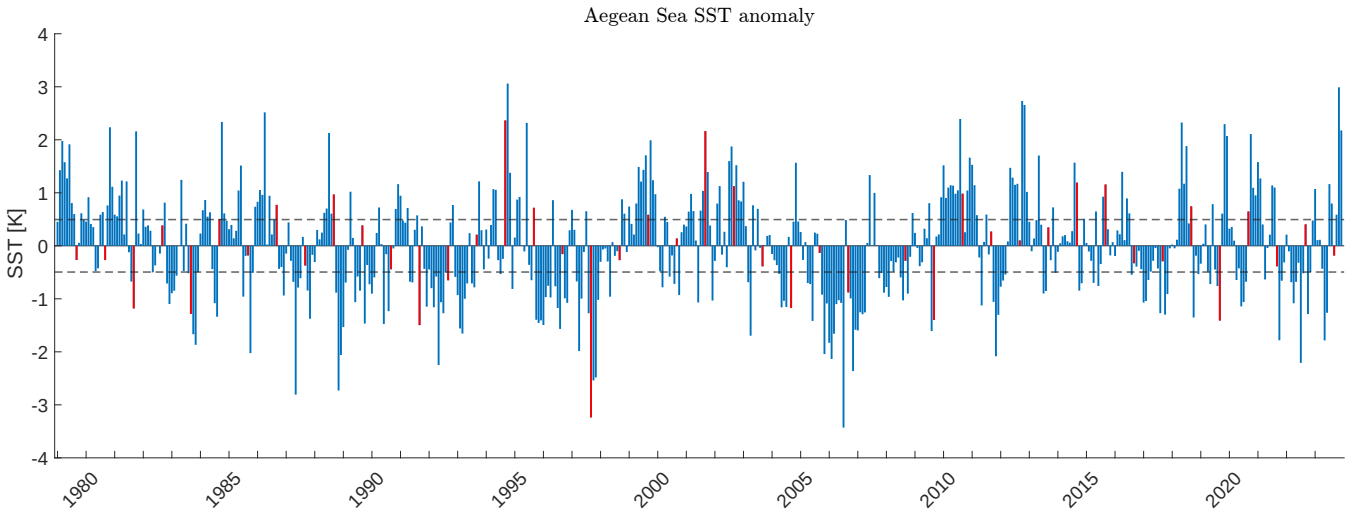

Figure S8. Aegean Sea detrended SST anomaly timeseries.

AQA lagged correlation to Levant land precipitation

	Jul	Aug	Sep	Oct	Nov
ERA5 NDJFM	0.25	**-0.51**	0.09	0.10	-0.14
ERA5 DJF	0.18	**-0.60**	0.02	0.17	0.06
ERA5 NDJ	0.17	**-0.46**	-0.03	0.21	**-0.35**
ERA5 JFM	0.27	**-0.53**	0.11	-0.01	0.04
IMS DJF	0.16	**-0.41**	0.06	0.17	0.09
Nov	-0.02	0.02	0.14	0.14	**-0.66**
Dec	0.15	**-0.31**	-0.09	0.14	0.11
Jan	0.16	**-0.50**	-0.07	0.09	-0.15
Feb	0.04	**-0.37**	0.19	0.10	0.14
Mar	**0.32**	-0.12	0.07	-0.23	0.08

Figure S9. Correlations of AQA with Levant winter land precipitation for the months November–March, extending the lagged correlations shown in Figure 5b of the main text.

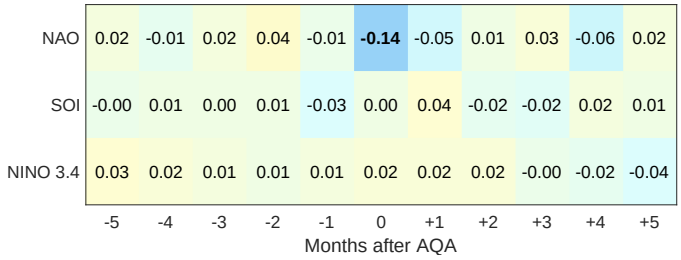

Figure S10. Lagged correlation of AQA and the North Atlantic Oscillation index (NAO), Southern Oscillation index (SOI), and SST anomaly in the NINO 3.4 region (NINO 3.4 index). NAO, SOI, and SST anomalies at NINO 3.4 were downloaded from *https://www.ncei.noaa.gov/access/monitoring/products/*. Based on index data availability, monthly NAO and SOI correlations are calculated for the period 1979–2023; and NINO 3.4 correlations calculated for the period 1982–2023.

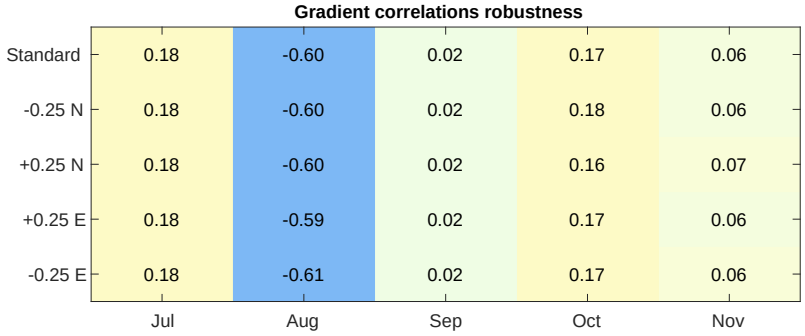

Figure S11. Calculating the robustness of the correlations of AQA and Levant winter precipitation by shifting the region used to define the Aegean Sea in the calculation of AQA to the North-South and East-West by $0.25°$.

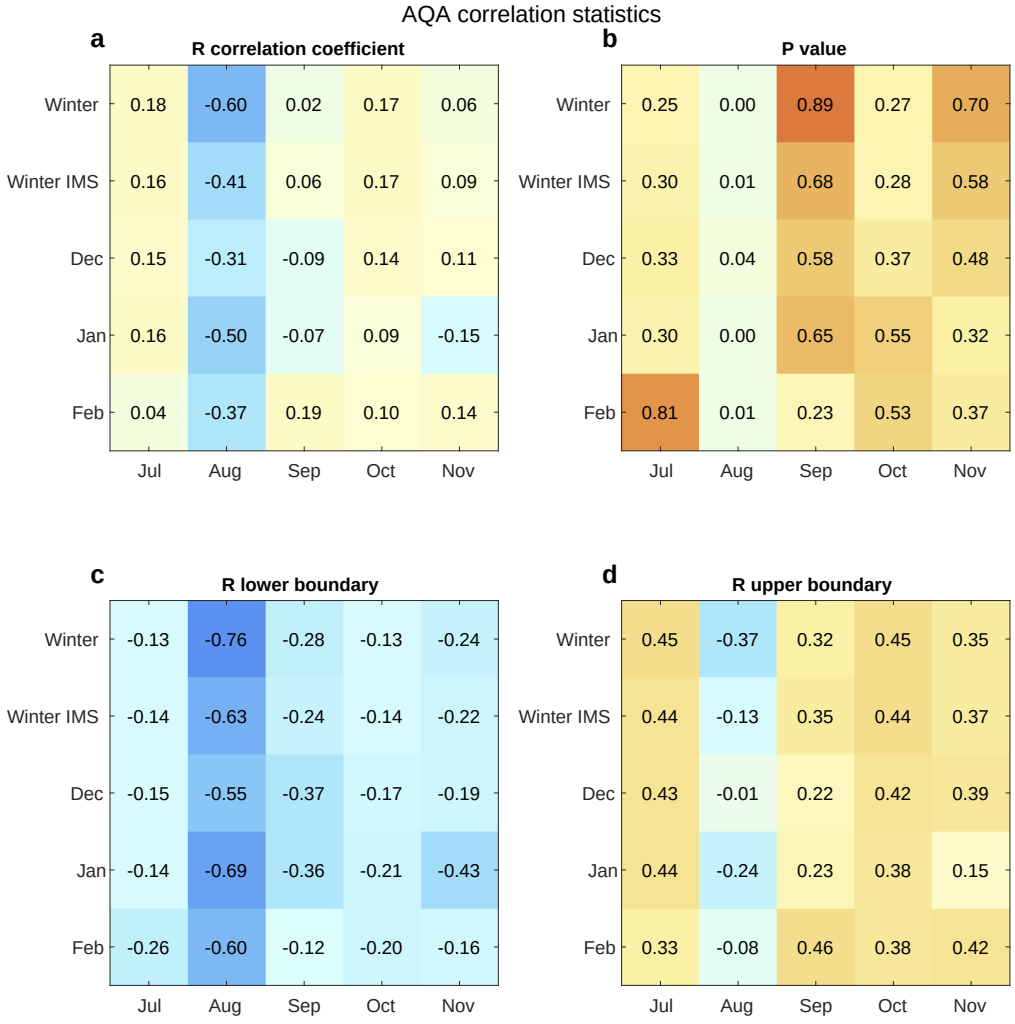

Figure S12. The statistics of the lagged correlations between AQA and winter precipitation in the Levant. (a) The R correlation coefficient between AQA and Levant winter precipitation; (b) P value of the correlation coefficient; (c) 95 percentile lower boundary for the R correlation coefficient; (d) 95 percentile upper boundary for the R correlation coefficient.

S4 Synoptic analysis

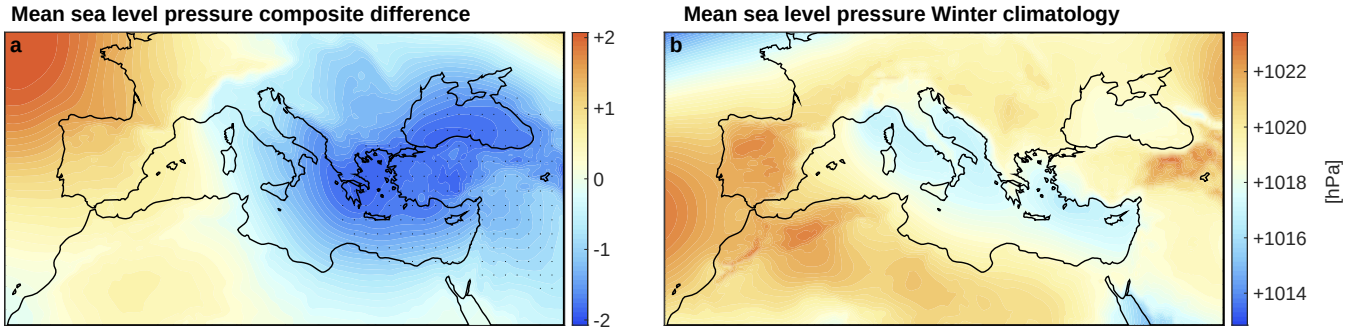

Figure S13. (a) Difference in monthly mean sea-level pressure during winter (Dec–Feb) between negative and positive AQA composites (i.e., AQA negative and positive values during the August preceding winter months). (b) The climatological mean winter mean sea-level pressure. Data taken from ERA5 for the years 1979–2023. Stippling indicates 95% confidence estimated using bootstrap.

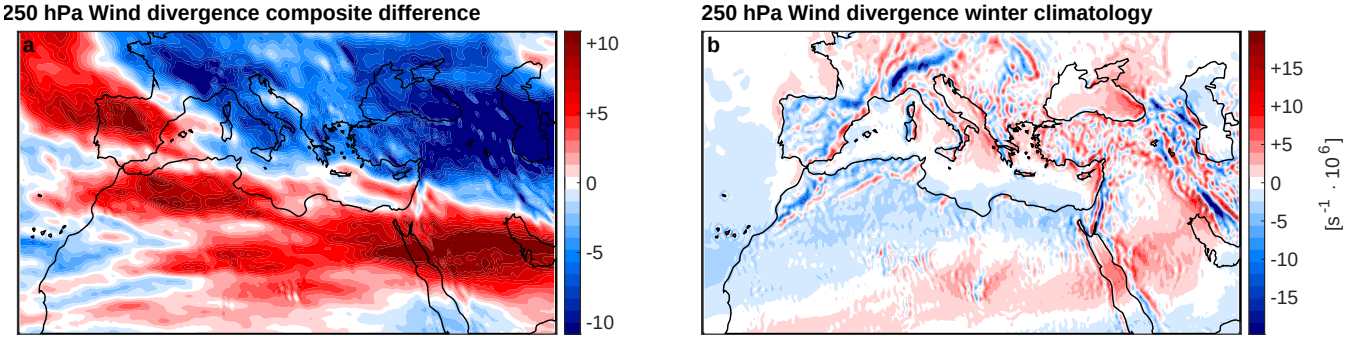

Figure S14. Wind divergence at the 250 hPa level. (a) Difference in 250 hPa wind divergence during winter (Dec–Feb) between negative and positive AQA composites (i.e., AQA negative and positive values during the August preceding winter months). (b) The climatological mean 250 hPa wind divergence during winter. Data taken from ERA5 for the years 1979–2023. Stippling indicates 95% confidence estimated using bootstrap.